

Gated2Depth: Real-time Dense Lidar from Gated Images

Tobias Gruber

Frank Julca-Aguilar

Mario Bijelic

Werner Ritter

Klaus Dietmayer

Felix Heide

Abstract

We present an imaging framework which converts three images from a gated camera into high-resolution depth maps with depth resolution comparable to pulsed lidar measurements. Existing scanning lidar systems achieve low spatial resolution at large ranges due to mechanically-limited angular sampling rates, restricting scene understanding tasks to close-range clusters with dense sampling. In addition, today's lidar detector technologies, short-pulsed laser sources and scanning mechanics result in high cost, power consumption and large form-factors. We depart from point scanning and propose a learned architecture that recovers high-fidelity dense depth from three temporally gated images, acquired with a flash source and a high-resolution CMOS sensor. The proposed architecture exploits semantic context across gated slices, and is trained on a synthetic discriminator loss without the need of dense depth labels. The method is real-time and essentially turns a gated camera into a low-cost dense flash lidar which we validate on a wide range of outdoor driving captures and in simulations.

1. Introduction

Active depth cameras, such as scanning lidar systems, have not only become a cornerstone imaging modality for autonomous driving and robotics, but also are emerging in applications across disciplines, including autonomous drones, remote sensing, human-computer interaction, and augmented or virtual reality. Depth cameras that provide dense range measurements allow for dense scene reconstructions [28] when combined with conventional color cameras, including correlation time-of-flight cameras (C-ToF) [38, 35, 22] such as Microsoft's Kinect One, or structured light cameras [56, 47, 46, 2]. As a result, these acquisition systems facilitate the collection of large-scale RGB-D data sets that fuel 3D deep learning for core problems in computer vision, including scene understanding [60, 26] and action recognition [44]. However, while these existing depth cameras provide high-fidelity depth for close ranges in indoor environments [28, 43], dense depth imaging at long ranges and in dynamic outdoor scenarios is an open

challenge.

Active imaging at long ranges is challenging because diffuse scene points only return a small fraction of the emitted photons back to the sensor. For perfect Lambertian surfaces, this fraction decreases quadratically with distance, posing a fundamental limitation as illumination power can only be increased up to the critical eye-safety level [57, 61, 66]. To tackle this constraint, existing pulsed lidar systems employ sensitive silicon avalanche photo-diodes (APDs) with high photon detection efficiency in the NIR band [66]. The custom semiconductor process for these sensitive detectors restricts current lidar systems to single (or few) APDs instead of monolithic sensor arrays, demanding point-by-point scanned acquisition driving cost, footprint. Although scanning lidar approaches facilitate depth imaging at large ranges, scanning reduces their spatial resolution quadratically with distance, prohibiting semantic tasks for far objects as shown in Fig. 1. Recently, single-photon avalanche diodes (SPADs) [4, 52, 45, 5] are emerging as a promising technology that may enable sensor arrays in the CMOS process [12] in the future. Although SPADs are sensitive to individual photons, existing designs are highly photon-inefficient due to very low fill factors around 1% [65] and pileup distortions at higher pulse powers [12]. Moreover, passive depth estimation techniques do not offer a solution, including stereo cameras [56, 23] and depth from monocular imagery [55, 14, 19]. These approaches perform poorly at large ranges due to small disparity or ambiguous semantics at distance, and fail in critical outdoor scenarios, when ambient light is not sufficient, e.g. overcast days or at night, and in the presence of strong back-scatter, e.g. in fog, rain or snow, see Fig. 2.

Gated imaging is an emerging sensing technology that tackles these challenging scenarios by sending out pulsed illumination and integrating a scene response between temporal gates. Coarse temporal slicing allows for the removal of back-scatter due to fog, rain and snow, and can be realized in readily available CMOS technology. In contrast to existing pulsed lidar systems, gated imaging offers high signal measurements at long distances by integrating incoming photons over large temporal slice, instead of time-tagging the first returns of individual pulses. However, although gated cameras offer an elegant, low-cost solution to challenging outdoor imaging scenarios, the sequential acquisi-

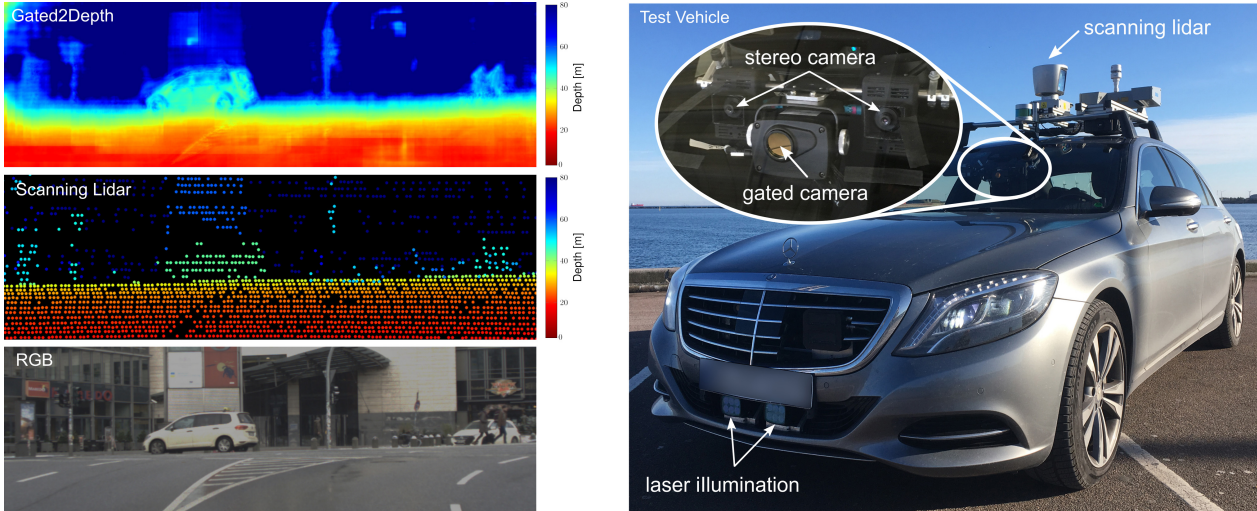


Figure 1: We propose a novel real-time framework for dense depth estimation (top-left) without scanning mechanisms. Our method maps measurements from a flood-illuminated gated camera behind the wind-shield (inset right), captured in real-time, to dense depth maps with depth accuracy comparable to lidar measurements (center-left). In contrast to the sparse lidar measurements, these depth maps are high-resolution enabling semantic understanding at long ranges. We evaluate our method on synthetic and real data, collected with a testing and a scanning lidar Velodyne HDL64-S3D as reference (right).

tion of the individual slices prohibits their use as depth cameras today, restricting depth information to a sparse set of wide temporal bins spanning more than 50 meters in depth. Note that using narrow slices does not offer a solution, because the gate width is inversely proportional to the number of captures, and thus frame-rate, needed to cover a given depth range. With maximum capture frame rates of 120 Hz to 240 Hz existing systems [21] are restricted to 4 to 7 slices for dynamic scenes.

In this work, we present a method that recovers high-fidelity dense depth and reflectance from sparse gated images. By learning to exploit semantic context across gated slices, the proposed architecture achieves depth resolution comparable to scanning based lidar in large-range outdoor scenarios, essentially turning a gated camera into a low-cost dense flash lidar that also sees through fog, snow and rain. The method jointly solves depth estimation, denoising, inpainting of missing or unreliable measurements, shadow and multi-path removal, while being highly efficient with interactive frame rates on consumer GPUs.

Specifically, we make the following contributions:

- We propose a learning-based approach for estimating dense depth from gated images, without the need of dense depth labels for training.
- We validate the proposed method in simulation and on measurements acquired with a prototype system in challenging automotive imaging scenarios. We show that the method recovers dense depth up to 100m with depth resolution comparable to scanning lidar.

- We introduce a synthetic data set with dense depth labels, and measured data set with sparse Lidar point estimates. The data sets and model will be published for full reproducibility.

2. Related Work

Depth Estimation from Intensity Images A large body of work explores methods for extracting depth from conventional color image sensors. A first line of research on structure from motion methods sequentially captures a stack of single camera images and extracts geometry by exploiting temporal correlation in the stack [34, 63, 64, 69]. In contrast, multi-view depth estimation methods [23] do not rely on sequential acquisition but exploit the disparity between corresponding pixels in simultaneously acquired images from camera pairs [58]. Recent approaches to estimating stereo correspondences allow for interactive frame-rates by proposing efficient convolutional neural network (CNN) architectures [32, 8, 48]. Over the last years, a promising direction of research aims at estimating depth from single monocular images [55, 14, 37, 19, 9], no longer requiring multi-view or sequential captures. Saxena et al. [55] introduce a Markov Random Field that is capable to incorporate multiscale local and global image features for depth estimation. Eigen et. al [14] demonstrate that CNNs are well-suited for monocular depth estimation by learning priors on semantic-dependent depth [37, 10, 19]. While consumer time-of-flight cameras facilitate acquisition of large datasets for small indoor scenes [60, 26], supervised training in large outdoor environments is an open challenge. Re-

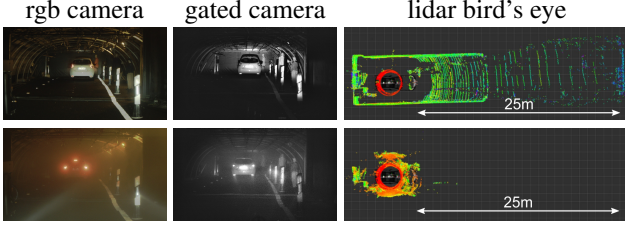


Figure 2: Sensor performance in a fog chamber with very dense fog. The first row shows reference recordings without fog while the second row shows the same scene in very foggy conditions.

cent approaches tackle the lack of dense training data by proposing semi-supervised methods relying either on relative depth [10], stereo images [17, 36, 19], sparse lidar points [36] or semantic labels [49]. Existing methods relying solely on color imagery have in common that their precision is more than an order of magnitude below the accuracy of scanning lidar systems which makes these methods no valid low-cost alternative to ubiquitous lidar ranging in autonomous robotic applications [57]. In this work, we propose a method that allows to close this precision gap using low-cost gated imagers.

Sparse Depth Completion As an alternative approach to recover accurate dense depth, a recent line of work proposes depth completion from the sparse lidar measurements. Similar to monocular depth estimation, learned encoder-decoder architectures have been proposed for this task [41, 11, 29]. Jaritz et al. [29] propose to incorporate color RGB data for upsampling sparse depth samples but also require sparse depth samples in down-stream scene understanding tasks. To allow for independent design of depth estimation and scene analysis network components, the completion architecture has to be trained with varying sparsity patterns [41, 29] or additional validity maps [11]. However, while these existing lidar completion methods offer improved depth estimates, they suffer from same limitation of the scanned lidar sensors: low spatial resolution at long ranges due to limited angular sampling rates, custom low-resolution detectors, and high-cost mechanical scanning.

Time-of-Flight Depth Cameras Amplitude-modulated C-ToF cameras [38, 35, 22], such as Microsoft’s Kinect One, have become broadly adopted for dense depth sensing in indoor scenarios [60, 26]. These cameras measure depth by recording the phase shift of periodically-modulated flood light illumination, which allows to extract the time-of-flight for the reflected flood light from the source to scene and back to the camera. In contrast to pulsed time-of-flight cameras [4, 5], C-ToF cameras can be manufactured in mixed CCD/CMOS technology [38] as megapixel arrays and do

not require costly scanning mechanics or optics [22]. However, in addition to the modulated light, this sensing approach also records all ambient background light. While per-pixel lock-in amplification removes background components efficiently in indoor scenarios [38], and learned architectures can alleviate multi-path distortions [62], existing C-ToF cameras are limited to ranges of a few meters in outdoor scenarios [25] with strong sunlight illumination present.

Instead of continuously integrating, gated cameras send out pulses of flood-light and only record photons from a certain distance by opening and closing the camera after a given delay. Gated imaging has been first proposed by Heckman et al. [24]. This acquisition mode allows to gate out ambient light, and back-scatter from fog, rain, and snow, making it a promising technology for outdoor imaging [21] in harsh scenarios. Busck et al. [7, 6, 3] adopt gated imaging for high-resolution depth sensing by capturing large sequences of narrow gated slices. However, as the depth accuracy is inversely related to the gate width, and hence the number of required captures, sequentially capturing high-resolution gated depth is infeasible at real-time frame-rates. Recently, a line of research proposes analytic reconstruction models for known pulse and integration shapes [40, 39, 67]. In the overlapping region of at least two trapezoidal slices, distance can be estimated according to the correlation of the intensities in all slices. However, these range-intensity correlation methods require perfect prior knowledge of the integration and pulse profiles, which is impractical due to drift in the laser and gate shape profiles, and they provide low precision for broad overlaps in real-time capture settings. In this work, we demonstrate that exploiting scene semantics allows to recover dense and lidar-accurate depth from only three slices acquired in real-time.

3. Gated Imaging

In this section, we review gated imaging and propose an analytic per-pixel depth estimation method.

Gated Imaging We consider the setup shown in Fig. 3, where an amplitude-modulated source flood-illuminates the scene with broad rect-shaped “pulses” of light. The synchronized camera opens after a designated delay t_0 to receive only photons with round-trip path-length longer than $t_0 \cdot c$, where c is the speed of light. Following [3], after starting the exposure at t_0 , the detector gain is temporally modulated with the gating function g resulting in the exposure measurement

$$I(t_0) = \int_{-\infty}^{\infty} g(t - t_0) \kappa(t) dt. \quad (1)$$

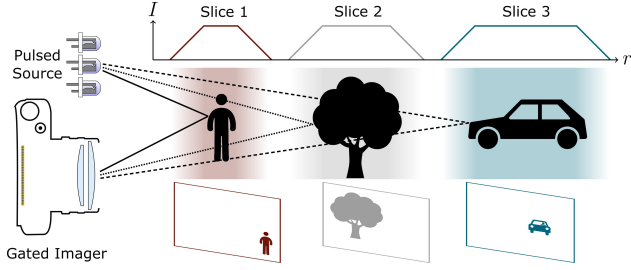


Figure 3: A gated system consists of a pulsed laser source and a gated imager that are time synchronized. By setting the delay between illumination and image acquisition, the environment can be sliced into single images that contain only a certain distance range.

where κ is the temporal scene response. Assuming a single direct reflection at distance r , the temporal scene response can be described as

$$\kappa(t) = p\left(t - \frac{2r}{c}\right) \alpha \beta(r). \quad (2)$$

where p is here the laser pulse profile, α is the albedo of the target, and atmospheric effects, e.g. in a scattering medium, is modeled by the distance-dependent function β . Note that we ignore ambient light in Eq. (2) as this offset is minimized by a notch-filter setup and eliminated by subtraction with a separate capture without active illumination.

For a fixed slice with delay t_0 , the correlation measurement I_{t_0} characterizes the pixel intensity with respect to distance r . If the laser pulse and detector gain are rectangular with duration t_L and t_G , respectively, $I_{t_0}(r)$ is trapezoidal in r as shown in Fig. 3 and Fig. 4. Note, that the ratio of two gated measurements I_{t_0} and I_{t_1} is scene-independent except for the depth r

$$\frac{I_{t_0}}{I_{t_1}} = \frac{\int_{-\infty}^{\infty} g(t - t_0) p\left(t - \frac{2r}{c}\right) dt}{\int_{-\infty}^{\infty} g(t - t_1) p\left(t - \frac{2r}{c}\right) dt}, \quad (3)$$

The final measurement, after read-out, is affected by photon shot noise and read-out noise as

$$z(r) = I_{t_0}(r) + \eta_p(I_{t_0}(r)) + \eta_g, \quad (4)$$

for a given pixel location, with η_p being a Poissonian signal-dependent noise component and η_g a Gaussian signal-independent component, which we adopt from [15].

Analytical Per-Pixel Depth from Gated Image Slices.

As a baseline, we propose an analytic depth estimation

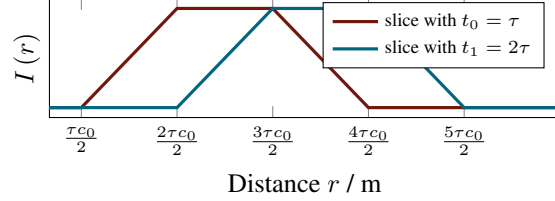


Figure 4: Example exposure profiles for varying distance r with rectangular gate of length $t_G = 2\tau$ and rectangular pulse of width $t_L = \tau$.

method inspired by [40], which relies on overlapping regions between neighboring gated slices. Next, we consider two overlapping gates with identical laser duration $t_L = \tau$ and gate duration $t_G = 2\tau$ and, but different delays $t_0 = \tau$ and $t_1 = 2\tau$, respectively. As shown in Fig. 4, the two corresponding slices $I_{t_0}(r)$ and $I_{t_1}(r)$ are trapezoidal and overlapping in $\frac{2\tau c_0}{2} \leq r \leq \frac{4\tau c_0}{2}$. For points in the range $[2\tau c, 4\tau c]$, we can estimate their depth as

$$\hat{r} = \begin{cases} \frac{c}{2} \left(2\tau + \frac{I_{t_0}}{I_{t_1}} \tau \right) & \text{for } \frac{2\tau c}{2} \leq r \leq \frac{3\tau c}{2} \\ \frac{c}{2} \left(3\tau + \frac{I_{t_1}}{I_{t_0}} \tau \right) & \text{for } \frac{3\tau c}{2} < r \leq \frac{4\tau c}{2} \end{cases}. \quad (5)$$

However, this approach assumes that we know the corresponding overlapping slices for every pixel, which unfortunately requires again knowing the scene depth. As a rough scene prior, we select the mean distance of the slice with maximum intensity in all comparisons throughout the remainder of this work.

Measurement Distortions In addition to unknown slice correspondence, a number of systematic and random measurement distortions make depth estimation from gated images challenging. Scene objects with low reflectance only return few signal photons, which makes ratio estimation according to Eq. (5) a challenge in the presence of the Poissonian-Gaussian measurement fluctuations from Eq. (4). Systematic distortions include multi-path bounces of the flash illumination, see also [62]. In typical driving scenarios, severe multi-path reflection can occur due to wet roads acting as mirroring surfaces in the scene. Note that these are almost negligible in line or point-based scanning-lidar systems [1]. Furthermore, due to different mounting positions of laser and camera, shadows appear behind objects and make estimation behind impossible. While a narrow notch-filter reduces ambient illumination effects, severe ambient sunlight, present as an offset in all slices, reduces the dynamic range of the gated measurements. In the following, we demonstrate a reconstruction architecture which addresses all of these issues in a data-driven approach, relying on readily available sparse lidar depth as training labels.

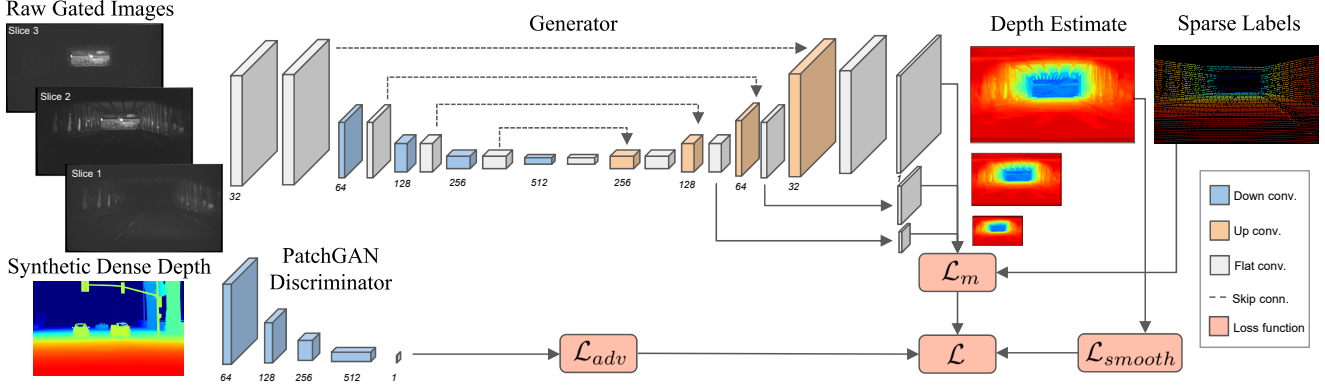


Figure 5: The proposed GATED2DEPTH architecture estimates dense depth from a set of three gated images (actual reconstruction and real captures shown). To train the proposed generator network G using sparse depth from lidar point samples, we rely on three loss-function components: a sparse multi-scale loss \mathcal{L}_m which penalizes sparse depth difference on three different binned scales, a smoothness loss \mathcal{L}_{smooth} , and an adversarial loss \mathcal{L}_{adv} . The adversarial loss incorporates a discriminator network which was trained on synthetic data, using a separate throw-away generator, and allows to transfer dense depth details from synthetic data without domain adaptation.

4. Learning Depth from Gated Images

We introduce the *Gated2DepthNet* network which estimates dense high-quality depth maps from three gated images. The proposed network’s architecture is illustrated in Fig. 5. The input to our network are three gated slices. By design, the gated channels encode depth information through coded illumination in the NIR range, suppressing most ambient illumination by notch-filtering and high peak-power. The proposed network exploits the corresponding semantics across the gated images to generate an accurate a pixel-wise depth estimation.

An essential difficulty when designing a dense depth estimation technique for long ranges is the lack of dense ground truth depth for training. This issue becomes crucial when designing deep models, which require a large training corpus. We overcome this problem by a training strategy that transfers dense depth semantics learned on synthetic data to a network trained on sparse lidar data.

Specifically, the proposed *Gated2DepthNet* is composed of a generator, G , which we train for our dense depth estimation task. G is a multi-scale variant of the popular U-net [53] architecture. To transfer dense depth from synthetically generated depth maps to sensor data, we introduce a discriminator D , a variant of PatchGAN [27], and train the network in a two-stage process. In the first stage, we train a network (G and D) on synthetic data as generative adversarial network [20]. The generator and discriminator are trained alternately using a least square GAN [42] approach: G is trained to generate accurate dense depth estimations (using synthetic groundtruth) and to convince D that the estimations correspond to a real depth maps; D is trained to detect whether a dense depth map comes from G

or is a real one. In the second stage, we train the network on real gated images that follow the target domain distribution. We now use sparse lidar measurements as groundtruth and keep the discriminator fixed. To utilize sparse lidar measurements in the final training stage, we introduce a multi-scale loss (see Section 4.1) that penalizes binned differences to sparse lidar points at multiple feature map scales.

Our generator U-net variant consists of 4 pairs of convolutions, having a max pooling operation after each pair. As a result of these operations, the encoder produces internal maps of $\frac{1}{2}$, $\frac{1}{4}$, $\frac{1}{8}$, and $\frac{1}{16}$ of the original input size. The decoder consists of four additional convolutions, and transposed convolutions after each pair. As the expected estimation map shares structural characteristics with the input, we also rely on skip connections, placed symmetrically, as illustrated in Fig. 5.

For the discriminator architecture, we aim at enforcing modeling of high-frequency structures through a PatchGAN variant. To this end, we define a fully convolutional network with five layers. The network classifies overlapping patches of a dense depth map instead of the whole map. As a result, the network generates a new map with a classification for each of the different processed patches of the input. The proposed discriminator is able to efficiently process input of variable sizes and, as the number of parameters is much smaller than a conventional GAN, allows to easier training.

4.1. Loss Function

We train our proposed network to minimize a three component loss function, \mathcal{L} , each modeling different statistics of the target depth, defined as:

$$\mathcal{L} = \mathcal{L}_{mult} + \lambda_s \mathcal{L}_{smooth} + \lambda_a \mathcal{L}_{adv} \quad (6)$$

4.1.1 Multi-scale loss (\mathcal{L}_{mult})

This loss component penalizes differences between the ground truth labels and the depth estimates. We define \mathcal{L}_{mult} as a multi-scale loss over the generator's output, d , and its corresponding target, \tilde{d} :

$$\mathcal{L}_{mult}(d, \tilde{d}) = \sum_{i=1}^M \lambda_{m_i} \mathcal{L}_{L1}(d^{(i)}, \tilde{d}^{(i)}) \quad (7)$$

where $d^{(i)}$ and $\tilde{d}^{(i)}$ are the generator's output and target at a scale (i) , $\mathcal{L}_{L1}(d^{(i)}, \tilde{d}^{(i)})$ is the loss at scale (i) , and λ_{m_i} is the weight of the loss at the same scale. We define three scales 2^i binning as illustrated in Fig. 5). For a scale (i) , we define $\mathcal{L}_{L1}(d^{(i)}, \tilde{d}^{(i)})$ as the mean absolute error:

$$\mathcal{L}_{L1}(d^{(i)}, \tilde{d}^{(i)}) = \frac{1}{N} \sum_{j,k} |d_{jk}^{(i)} - \tilde{d}_{jk}^{(i)}| \quad (8)$$

When training with synthetic data, we compute \mathcal{L}_{L1} over all pixels. For training with real data, we only compute this loss at the lidar sample positions. \mathcal{L}_{L1} is formally defined as:

$$\mathcal{L}_{L1}(d^{(i)}, \tilde{d}^{(i)}) = \frac{1}{N} \sum_{j,k} |d_{jk}^{(i)} - \tilde{d}_{jk}^{(i)}| m_{jk}^{(i)} \quad (9)$$

where $m_{jk} = 1$ for valid lidar measurements, and $m_{jk} = 0$ otherwise. For smaller scales, we down-sample each lidar map by dividing the map into bins and compute the average for each bin.

4.1.2 Weighted Smoothness Loss (\mathcal{L}_{smooth})

We rely on an additional smoothness loss \mathcal{L}_{smooth} to regularize the depth estimates. Specifically we use a total variation loss weighted by the input image gradients [49], that is

$$\mathcal{L}_{smooth} = \frac{1}{N} \sum_{i,j} |\partial_x d_{i,j}| e^{-|\partial_x z_{i,j}|} + |\partial_y d_{i,j}| e^{-|\partial_y z_{i,j}|}, \quad (10)$$

where z is here the input image. As sparse lidar data is sampled on horizontal lines due to the angular scanning, a generator trained over this data is biased to generate outputs with similar horizontal patterns. Incrementing the weight of the vertical gradient relative to the horizontal one helps to cope with this problem.

4.1.3 Adversarial loss (\mathcal{L}_{adv})

We define the adversarial loss following [42] with the patch-GAN [27] discriminator:

$$\mathcal{L}_{adv} = \frac{1}{2} \mathbb{E}_{y \sim p_{depth}(y)} [(D(y) - 1)^2] + \frac{1}{2} \mathbb{E}_{x \sim p_{gated}(x)} [(D(G(x)))^2] \quad (11)$$

Note that in the second stage of our training, we only use the fixed discriminator in the loss.

4.2. Training and Implementation Details

We use ADAM optimizer with the learning rate set to 0.0001. For the global loss function, we experimentally use $\lambda_s = 0.0001$ and $\lambda_a = 0.001$. For the multi-scale loss, we define $\lambda_{m_0} = 1$, $\lambda_{m_1} = 0.8$, and $\lambda_{m_2} = 0.6$. The inference rate of our trained model is 30 FPS on two TitanX GPUs.

5. Datasets

In this section, we describe the synthetic and real data sets used to train and evaluate the proposed method. As gated cameras are an emerging sensor modality, simulated data or captured data is not available in existing data sets [18], [68].

5.1. Synthetic Dataset

Recently, a large variety of synthetic datasets generated by advanced real-time game engines have emerged [54, 16, 51, 50, 30]. While these existing data sets contain RGB images and only sometimes depth maps, they do not contain enough information to synthesize realistic gated measurements that require NIR reflectance modeling and passive sunlight-illumination. We modify the GTA5-based simulation framework from [50] to address this issue. Using Renderdoc [31], every drawcall and buffer can be read out from the GPU while playing GTA5 [50]. Extracted data include diffuse reflectances, normal vectors, specular information, sunlight illumination, depth map, stencil and projection matrix [13].

We warp the GTA5 frame to match realistic extrinsic calibration parameters of our prototype acquisition system shown in Fig. 1. Matching the mounting position of the flash illumination allows us to accurately model the shadows in the experimental gated images (see also Fig. 6). The reflectance of the objects in the NIR regime is based on the diffuse RGB reflectance extended with a RGB to NIR model [33]. This conversion, as well as additional saturation and blooming modeling is described in the Supplemental Material. The gating function according to Eq. 1 and the Poissonian-Gaussian noise model from Eq. 4 is applied, where the gating and noise parameters are calibrated from a BrightwayVision BrightEye camera. We simulated 16909 samples, where we use 13541 for training, 1505 for validation and 997 for testing.

5.2. Real Dataset

For experimental validation, we have equipped a testing vehicle with a standard RGB stereo camera (Aptina AR0230), lidar system (Velodyne HDL64-S3) and a gated camera (BrightwayVision BrightEye) with flood-light

source integrated into the front bumper, shown in Fig. 1. Both cameras are mounted behind the windshield, while the lidar is mounted on the roof. The stereo cam runs at 30 Hz with a resolution of 1920x1080 pixels. The gated camera provides a resolution of 1280x720 at a framerate of 120 Hz, which we split up in three slices. The car is equipped with two vertical-cavity surface-emitting laser (VCSEL) modules, which are diffused, with a wavelength of 808 nm and a pulsed optical output peak power of 500 W each. Our reference lidar systems is running with 10 Hz and yields 64 lines. All sensors are calibrated and time-synchronized. During a two-week test drive in Germany, Denmark and Sweden, we recorded 11108 frames in different cities (Hamburg, Copenhagen, Gothenburg, Stockholm, Sundsvall, Kiel), which serve as training set (8932) and test set (2176) for evaluation. For fine-grained evaluation, we split the test data into separate daily (1432) and nightly (744) sets.

6. Experimentation

6.1. Evaluation Setting

We compare our approach to state-of-the art algorithms based on monocular RGB images [19, 36], stereo images [8, 48], RGB images in combination with sparse lidar points [41]. We also consider the monocular depth estimation approaches [19, 36] applied on the integral of the gated slices, i.e. an actively illumination scene image without temporal information, which we dub full gated image.

For the method of Godard et al. [19], we resized our images to the native size the model was trained on as we noticed a substantial drop in performance when changing resolution at test time. For all other algorithms, we did not observe this behavior and we used the full resolution images. In the simulated comparisons, we calibrated the sampling pattern of the experimental lidar system and use this pattern for the Sparse-to-dense [41] method.

We evaluate the methods over the metrics used in [14], namely RMSE, RMSE log, MAE, ARD and $\delta < 1.25$, $\delta < 1.25^2$, $\delta < 1.25^3$. On the synthetic dataset, we compute the metrics over the whole depth maps. On the real dataset, we compute the metrics only at the predicted pixels that correspond to measured sparse lidar points. Moreover, we evaluate all methods over an estimation in a 3-150 m distance range to not bias the evaluation to large outliers at extreme scene distances.

6.2. Results on synthetic dataset

Tab. 1 shows that our proposed method outperforms all other reference methods by a large margin. The second-best method is the depth completion based on lidar and RGB [41], which yields better results than monocular or stereo methods because sparse lidar ground truth samples are given as input to this method. While monocular ap-

Method	RMSE	RMSE log	ARD	MAE [m]	$\delta < 1.25$ [%]	$\delta < 1.25^2$ [%]	$\delta < 1.25^3$ [%]
Real Data Night (Evaluated on Lidar Ground Truth Points)							
ANALYTIC GATED DEPTH	23.00	0.95	1.50	17.43	16.29	32.71	49.96
DEPTH FROM MONO ON RGB [19]	14.63	0.51	0.34	7.86	41.02	74.35	85.17
DEPTH FROM MONO ON RGB [36]	16.89	0.77	0.64	10.96	21.08	41.60	59.61
DEPTH FROM MONO ON FULL GATED [19]	16.32	0.57	0.39	8.52	60.37	74.37	82.45
DEPTH FROM MONO ON FULL GATED [36]	18.58	0.85	0.60	12.63	14.17	29.70	48.02
DEPTH FROM STEREO [8]	14.90	0.70	0.97	12.86	5.59	14.12	74.40
DEPTH FROM STEREO [48]	14.08	0.48	0.34	7.32	50.33	76.22	86.76
SPARSE-TO-DENSE ON LIDAR (GT INPUT) [41]	6.94	0.22	0.14	2.78	91.17	95.14	96.83
OUR APPROACH	7.72	0.26	0.18	3.69	82.36	91.67	95.49
Real Data Day (Evaluated on Lidar Ground Truth Points)							
ANALYTIC GATED DEPTH	27.37	1.07	1.83	22.46	12.64	26.03	39.90
DEPTH FROM MONO ON RGB [19]	13.15	0.50	0.32	7.74	26.43	72.66	85.85
DEPTH FROM MONO ON RGB [36]	15.47	0.73	0.63	10.54	19.19	39.15	59.84
DEPTH FROM MONO ON FULL GATED [19]	13.12	0.47	0.24	6.79	64.79	78.54	86.22
DEPTH FROM MONO ON FULL GATED [36]	17.54	0.79	0.58	12.12	15.83	32.30	52.30
DEPTH FROM STEREO [8]	15.28	0.68	0.95	13.33	4.47	12.45	79.80
DEPTH FROM STEREO [48]	14.25	0.51	0.33	7.76	43.12	72.66	84.51
SPARSE-TO-DENSE ON LIDAR (GT INPUT) [41]	6.40	0.20	0.11	2.52	92.88	96.46	97.80
OUR APPROACH	8.93	0.31	0.23	4.96	68.36	88.40	94.46
Simulated Data (Evaluated on Dense Ground Truth Depth)							
ANALYTIC GATED DEPTH	98.28	2.98	0.89	79.57	8.41	12.32	14.44
DEPTH FROM MONO ON RGB [19]	73.95	1.32	0.64	57.21	10.37	17.24	31.76
DEPTH FROM MONO ON RGB [36]	85.98	1.61	0.74	67.80	13.13	23.73	31.45
DEPTH FROM FULL GATED [19]	85.32	1.57	0.76	69.33	2.73	7.09	18.12
DEPTH FROM FULL GATED [36]	92.17	1.91	0.77	74.13	8.20	16.22	22.99
DEPTH FROM STEREO [8]	69.34	1.40	0.71	56.68	7.59	16.28	27.23
DEPTH FROM STEREO [48]	72.47	1.33	0.65	55.55	10.56	21.02	36.28
SPARSE-TO-DENSE ON LIDAR (GT INPUT) [41]	68.71	1.16	0.38	46.55	54.63	59.93	63.74
OUR APPROACH	15.38	0.23	0.13	4.91	90.56	95.09	97.08

Table 1: Comparison of our proposed framework and state-of-the-art methods on unseen synthetic and real test data sets. GT INPUT: uses sparse ground truth as input.

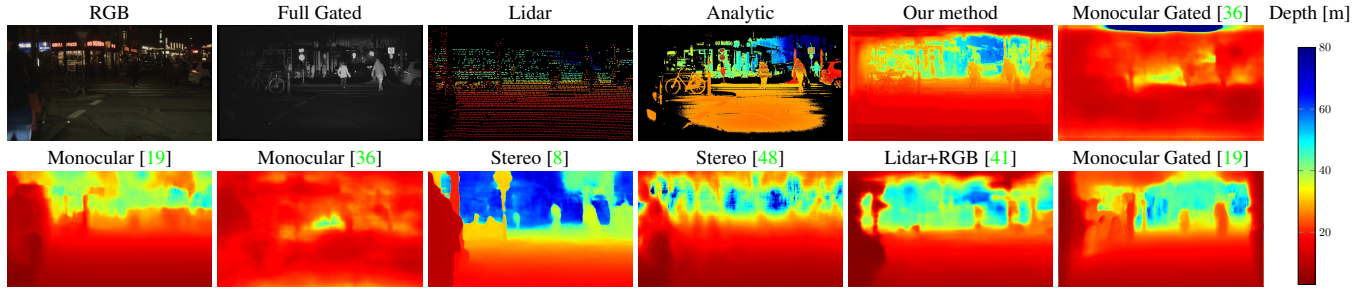
proaches have problems in estimating the absolute scale, stereo methods suffer from less quality right camera images due to required interpolation of occlusion areas.

Fig. 6c illustrates the highly accurate depth estimations of our method. The results show that our method is effective at capturing fine-grained details of a scene at both close and far distances.

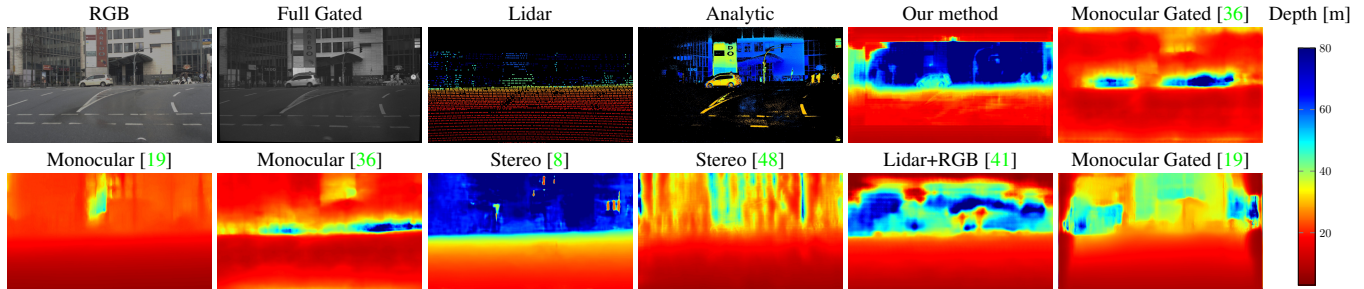
6.3. Results on real dataset

Tab. 1 shows that the proposed method outperform all methods without the ground truth lidar points as input, but is close to the sparse depth completion from [41]. In contrast to all other compared methods, this approach takes as input the ground truth lidar measurements (and RGB image), and in the experimental analysis we evaluate all methods only on the available sparse lidar measurements. Hence, the proposed method achieves high depth accuracy comparable to a scanning based lidar systems, while in contrast providing dense depth estimates.

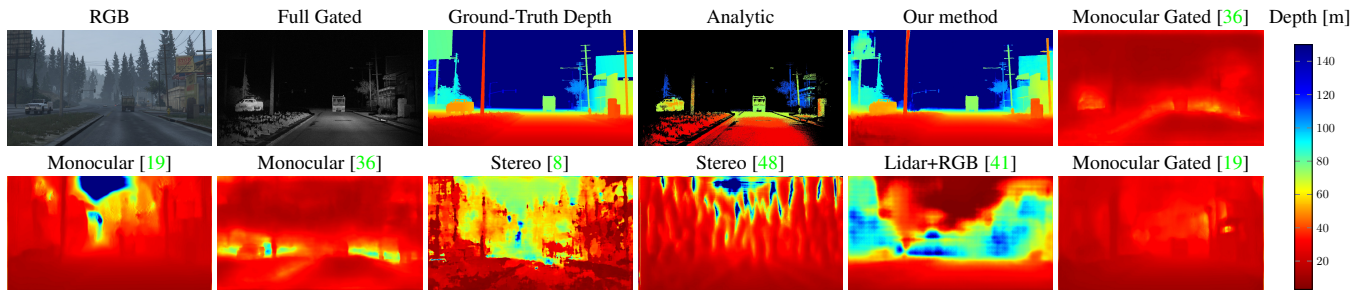
The qualitative results in Fig. 6a and Fig. 6b validate that our method is able to estimate dense, detailed scene depth, while stereo and monocular methods fail to provide fine detail. Especially for fine details around pedestrians or small scene objects, the proposed method achieves high resolution in contrast to all compared methods, allowing for semantic interpretations of these scene results even from the depth estimates only. Remaining artefacts are found at far off-axis regions close to the image boundaries which were not reached by the cone of active illumination and hence include no valid depth information. Note that the signal mag-



(a) Experimental night time results.



(b) Experimental day time results.



(c) Simulation results.

Figure 6: Qualitative results for our method and reference methods over real and synthetic examples. For each example, we include the corresponding RGB and full gated image, along with the lidar measurements. Our method generates more accurate and detailed maps over different distance ranges of the scenes in comparison to the other methods.

nitude is readily available in the measurements themselves as amplitude image, allowing to quantify the measurement uncertainty in such areas analogous to correlation time-of-flight methods [59]. However, as these peripheral areas can also be addressed with a wider cone of light, we do not address them specifically in the proposed method.

7. Conclusions and Future Work

In this work, we demonstrate a method to turn a CMOS gated camera into a cost-sensitive high-resolution dense flash lidar. We propose a novel way to transfer learning by extending real datasets with sparse depth labels with simulated dense ground truth depth. The proposed method overperforms state-of-the-art depth estimation methods, which we validate in simulations and experimentally on a wide range of outdoor captures with large depth range of up to

100 m.

An interesting direction for future research is the inclusion of RGB data, which could provide additional depth estimation clues in areas with little variational information in the gated images. However, fusing RGB images naively as an additional input channel to the proposed architecture would lead to severe bias for distortions due to backscatter, see Fig. 2, which are handled by the proposed system. A further exiting area of the proposed imaging modality are applications to large-scale semantic scene understanding and action recognition trained using the proposed architecture in an end-to-end-fashion.

References

- [1] S. Achar, J. R. Bartels, W. L. Whittaker, K. N. Kutulakos, and S. G. Narasimhan. Epipolar time-of-flight imaging. *ACM Transactions on Graphics (ToG)*, 36(4):37, 2017. 4
- [2] S. Achar, J. R. Bartels, W. L. R. Whittaker, K. N. Kutulakos, and S. G. Narasimhan. Epipolar time-of-flight imaging. *ACM Transactions on Graphics (ToG)*, 36(4):37:1–37:8, Jul 2017. 1
- [3] P. Andersson. Long-range three-dimensional imaging using range-gated laser radar images. *Optical Engineering*, 45(3):034301, 2006. 3
- [4] B. F. Aull, A. H. Loomis, D. J. Young, R. M. Heinrichs, B. J. Felton, P. J. Daniels, and D. J. Landers. Geiger-mode avalanche photodiodes for three-dimensional imaging. *Lincoln Laboratory Journal*, 13(2):335–349, 2002. 1, 3
- [5] D. Bronzi, Y. Zou, F. Villa, S. Tisa, A. Tosi, and F. Zappa. Automotive three-dimensional vision through a single-photon counting spad camera. *IEEE Transactions on Intelligent Transportation Systems*, 17(3):782–795, 2016. 1, 3
- [6] J. Busck. Underwater 3-D optical imaging with a gated viewing laser radar. *Optical Engineering*, 2005. 3
- [7] J. Busck and H. Heiselberg. Gated viewing and high-accuracy three-dimensional laser radar. *Applied Optics*, 43(24):4705–10, 2004. 3
- [8] J.-R. Chang and Y.-S. Chen. Pyramid stereo matching network. In *Proceedings of the IEEE Conference on Computer Vision and Pattern Recognition*, pages 5410–5418, 2018. 2, 7, 8
- [9] R. Chen, F. Mahmood, A. Yuille, and N. J. Durr. Rethinking monocular depth estimation with adversarial training. *arXiv preprint arXiv:1808.07528*, 2018. 2
- [10] W. Chen, Z. Fu, D. Yang, and J. Deng. Single-image depth perception in the wild. In D. D. Lee, M. Sugiyama, U. V. Luxburg, I. Guyon, and R. Garnett, editors, *Advances in Neural Information Processing Systems*, pages 730–738. Curran Associates, Inc., 2016. 2, 3
- [11] Z. Chen, V. Badrinarayanan, G. Drozdov, and A. Rabinovich. Estimating depth from rgb and sparse sensing. *arXiv preprint arXiv:1804.02771*, 2018. 3
- [12] P. Coates. The correction for photon ‘pile-up’ in the measurement of radiative lifetimes. *Journal of Physics E: Scientific Instruments*, 1(8):878, 1968. 1
- [13] A. Courrèges. GTAV - Graphics study. <http://www.adriancourreges.com/blog/2015/11/02/gta-v-graphics-study/>. 6
- [14] D. Eigen, C. Puhrsch, and R. Fergus. Depth map prediction from a single image using a multi-scale deep network. In *Advances in Neural Information Processing Systems*, pages 2366–2374, 2014. 1, 2, 7
- [15] A. Foi, M. Trimeche, V. Katkovnik, and K. Egiazarian. Practical Poissonian-Gaussian noise modeling and fitting for single-image raw-data. *IEEE Transactions on Image Processing*, 17(10):1737–1754, 2008. 4
- [16] A. Gaidon, Q. Wang, Y. Cabon, and E. Vig. Virtual worlds as proxy for multi-object tracking analysis. In *Proceedings of the IEEE Conference on Computer Vision and Pattern Recognition*, 2016. 6
- [17] R. Garg, V. K. B.G., G. Carneiro, and I. Reid. Unsupervised cnn for single view depth estimation: Geometry to the rescue. In *Proceedings of the IEEE European Conf. on Computer Vision*, pages 740–756, 2016. 3
- [18] A. Geiger, P. Lenz, and R. Urtasun. Are we ready for autonomous driving? the kitti vision benchmark suite. In *Computer Vision and Pattern Recognition (CVPR), 2012 IEEE Conference on*, pages 3354–3361. IEEE, 2012. 6
- [19] C. Godard, O. Mac Aodha, and G. J. Brostow. Unsupervised monocular depth estimation with left-right consistency. In *Proceedings of the IEEE Conference on Computer Vision and Pattern Recognition*, 2017. 1, 2, 3, 7, 8
- [20] I. Goodfellow, Y. Bengio, and A. Courville. *Deep Learning*. MIT Press, 2016. www.deeplearningbook.org. 5
- [21] Y. Grauer. Active gated imaging in driver assistance system. *Advanced Optical Technologies*, 3(2):151–160, 2014. 2, 3
- [22] M. Hansard, S. Lee, O. Choi, and R. P. Horaud. *Time-of-flight cameras: principles, methods and applications*. Springer Science & Business Media, 2012. 1, 3
- [23] R. Hartley and A. Zisserman. *Multiple view geometry in computer vision*. Cambridge university press, 2003. 1, 2
- [24] P. Heckman and R. T. Hodgson. 2.7Underwater Optical Range Gating. *IEEE Journal of Quantum Electronics*, 3(11):445–448, 1967. 3
- [25] F. Heide, W. Heidrich, M. Hullin, and G. Wetzstein. Doppler time-of-flight imaging. *ACM Transactions on Graphics (ToG)*, 34(4):36, 2015. 3
- [26] S. Hickson, S. Birchfield, I. Essa, and H. Christensen. Efficient hierarchical graph-based segmentation of rgbd videos. In *Proceedings of the IEEE Conference on Computer Vision and Pattern Recognition*, pages 344–351, 2014. 1, 2, 3
- [27] P. Isola, J.-Y. Zhu, T. Zhou, and A. A. Efros. Image-to-image translation with conditional adversarial networks. In *Proceedings of the IEEE Conference on Computer Vision and Pattern Recognition*, 2016. 5, 6
- [28] S. Izadi, D. Kim, O. Hilliges, D. Molyneaux, R. Newcombe, P. Kohli, J. Shotton, S. Hodges, D. Freeman, A. Davison, et al. Kinectfusion: real-time 3d reconstruction and interaction using a moving depth camera. In *Proceedings of the 24th annual ACM symposium on User interface software and technology*, pages 559–568, 2011. 1
- [29] M. Jaritz, R. De Charette, E. Wirbel, X. Perrotton, and F. Nashashibi. Sparse and dense data with cnns: Depth completion and semantic segmentation. In *International Conference on 3D Vision (3DV)*, pages 52–60, 2018. 3
- [30] M. Johnson-Roberson, C. Barto, R. Mehta, S. N. Sridhar, K. Rosaen, and R. Vasudevan. Driving in the matrix: Can virtual worlds replace human-generated annotations for real world tasks? In *IEEE International Conference on Robotics and Automation*, pages 1–8, 2017. 6
- [31] B. Karlsson. RenderDoc. <http://renderdoc.org>. 6
- [32] A. Kendall, H. Martirosyan, S. Dasgupta, P. Henry, R. Kennedy, A. Bachrach, and A. Bry. End-to-end learning of geometry and context for deep stereo regression. In *Proceedings of the IEEE International Conference on Computer Vision*, 2017. 2

- [33] M. Kennedy. How to create an infrared effect in photoshop. <https://digital-photography-school.com/create-infrared-effect-photoshop>. 6
- [34] J. J. Koenderink and A. J. Van Doorn. Affine structure from motion. *JOSA A*, 8(2):377–385, 1991. 2
- [35] A. Kolb, E. Barth, R. Koch, and R. Larsen. Time-of-flight cameras in computer graphics. In *Computer Graphics Forum*, volume 29, pages 141–159. Wiley Online Library, 2010. 1, 3
- [36] Y. Kuznietsov, J. Stückler, and B. Leibe. Semi-supervised deep learning for monocular depth map prediction. In *Proceedings of the IEEE Conference on Computer Vision and Pattern Recognition*, pages 2215–2223, 2017. 3, 7, 8
- [37] I. Laina, C. Rupprecht, V. Belagiannis, F. Tombari, and N. Navab. Deeper depth prediction with fully convolutional residual networks. In *International Conference on 3D Vision (3DV)*, pages 239–248, 2016. 2
- [38] R. Lange. 3d time-of-flight distance measurement with custom solid-state image sensors in cmos/ccd-technology. 2000. 1, 3
- [39] M. Laurenzis, F. Christnacher, N. Metzger, E. Bacher, and I. Zielenski. Three-dimensional range-gated imaging at infrared wavelengths with super-resolution depth mapping. In *SPIE Infrared Technology and Applications XXXV*, volume 7298, 2009. 3
- [40] M. Laurenzis, F. Christnacher, and D. Monnin. Long-range three-dimensional active imaging with superresolution depth mapping. *Optics Letters*, 32(21):3146–8, 2007. 3, 4
- [41] F. Ma and S. Karaman. Sparse-to-dense: Depth prediction from sparse depth samples and a single image. In *IEEE International Conference on Robotics and Automation*, pages 1–8, 2018. 3, 7, 8
- [42] X. Mao, Q. Li, H. Xie, R. Y. Lau, Z. Wang, and S. P. Smolley. Least squares generative adversarial networks. In *Proceedings of the IEEE International Conference on Computer Vision*, 2017. 5, 6
- [43] R. A. Newcombe, D. Fox, and S. M. Seitz. Dynamicfusion: Reconstruction and tracking of non-rigid scenes in real-time. In *Proceedings of the IEEE Conference on Computer Vision and Pattern Recognition*, Jun 2015. 1
- [44] B. Ni, G. Wang, and P. Moulin. Rgb-d-hudaact: A color-depth video database for human daily activity recognition. In *Consumer Depth Cameras for Computer Vision*, pages 193–208. Springer, 2013. 1
- [45] C. Niclass, A. Rochas, P.-A. Besse, and E. Charbon. Design and characterization of a cmos 3-d image sensor based on single photon avalanche diodes. *IEEE Journal of Solid-State Circuits*, 40(9):1847–1854, 2005. 1
- [46] M. O’Toole, F. Heide, L. Xiao, M. B. Hullin, W. Heidrich, and K. N. Kutulakos. Temporal frequency probing for 5d transient analysis of global light transport. *ACM Transactions on Graphics (ToG)*, 33(4):87, 2014. 1
- [47] M. O’Toole, R. Raskar, and K. N. Kutulakos. Primal-dual coding to probe light transport. *ACM Transactions on Graphics (ToG)*, 31(4):39–1, 2012. 1
- [48] A. Pilzer, D. Xu, M. Puscas, E. Ricci, and N. Sebe. Unsupervised adversarial depth estimation using cycled generative networks. In *International Conference on 3D Vision (3DV)*, pages 587–595, 2018. 2, 7, 8
- [49] P. Z. Ramirez, M. Poggi, F. Tosi, S. Mattoccia, and L. D. Stefano. Unsupervised monocular depth estimation with left-right consistency. In *Proceedings of the Asian Conference on Computer Vision*, 2018. 3, 6
- [50] S. R. Richter, Z. Hayder, and V. Koltun. Playing for benchmarks. In *Proceedings of the IEEE International Conference on Computer Vision*, pages 2232–2241, 2017. 6
- [51] S. R. Richter, V. Vineet, S. Roth, and V. Koltun. Playing for data: Ground truth from computer games. In B. Leibe, J. Matas, N. Sebe, and M. Welling, editors, *Proceedings of the IEEE European Conf. on Computer Vision*, volume 9906 of *LNCS*, pages 102–118. Springer International Publishing, 2016. 6
- [52] A. Rochas, M. Gosch, A. Serov, P. Besse, R. Popovic, T. Lasser, and R. Rigler. First fully integrated 2-d array of single-photon detectors in standard cmos technology. *IEEE Photonics Technology Letters*, 15(7):963–965, 2003. 1
- [53] O. Ronneberger, P. Fischer, and T. Brox. U-net: Convolutional networks for biomedical image segmentation. In *International Conference on Medical image computing and computer-assisted intervention*, pages 234–241. Springer, 2015. 5
- [54] G. Ros, L. Sellart, J. Materzynska, D. Vazquez, and A. M. Lopez. The synthia dataset: A large collection of synthetic images for semantic segmentation of urban scenes. In *Proceedings of the IEEE Conference on Computer Vision and Pattern Recognition*, Jun 2016. 6
- [55] A. Saxena, S. H. Chung, and A. Y. Ng. Learning depth from single monocular images. In *Advances in neural information processing systems*, pages 1161–1168, 2006. 1, 2
- [56] D. Scharstein and R. Szeliski. High-accuracy stereo depth maps using structured light. In *Proceedings of the IEEE Conference on Computer Vision and Pattern Recognition*, volume 1, pages I–I, 2003. 1
- [57] B. Schwarz. Lidar: Mapping the world in 3d. *Nature Photonics*, 4(7):429, 2010. 1, 3
- [58] S. M. Seitz, B. Curless, J. Diebel, D. Scharstein, and R. Szeliski. A comparison and evaluation of multi-view stereo reconstruction algorithms. In *Proceedings of the IEEE Conference on Computer Vision and Pattern Recognition*, pages 519–528, 2006. 2
- [59] S. Shrestha, F. Heide, W. Heidrich, and G. Wetzstein. Computational imaging with multi-camera time-of-flight systems. *ACM Transactions on Graphics (ToG)*, 35(4):33, 2016. 8
- [60] S. Song, S. P. Lichtenberg, and J. Xiao. Sun rgb-d: A rgb-d scene understanding benchmark suite. In *Proceedings of the IEEE Conference on Computer Vision and Pattern Recognition*, pages 567–576, 2015. 1, 2, 3
- [61] J. D. Spinhirne, J. A. RALL, and V. S. SCOTT. Compact eye safe lidar systems. *The Review of Laser Engineering*, 23(2):112–118, 1995. 1
- [62] S. Su, F. Heide, G. Wetzstein, and W. Heidrich. Deep end-to-end time-of-flight imaging. In *Proceedings of the IEEE Conference on Computer Vision and Pattern Recognition*, pages 6383–6392, 2018. 3, 4

- [63] P. H. Torr and A. Zisserman. Feature based methods for structure and motion estimation. In *International workshop on vision algorithms*, pages 278–294. Springer, 1999. 2
- [64] B. Ummenhofer, H. Zhou, J. Uhrig, N. Mayer, E. Ilg, A. Dosovitskiy, and T. Brox. DeMoN: Depth and Motion Network for Learning Monocular Stereo. In *Proceedings of the IEEE Conference on Computer Vision and Pattern Recognition*, 2017. 2
- [65] C. Veerappan, J. Richardson, R. Walker, D.-U. Li, M. W. Fishburn, Y. Maruyama, D. Stoppa, F. Borghetti, M. Gersbach, R. K. Henderson, et al. A 160×128 single-photon image sensor with on-pixel 55ps 10b time-to-digital converter. In *Solid-State Circuits Conference Digest of Technical Papers (ISSCC), 2011 IEEE International*, pages 312–314, 2011. 1
- [66] G. M. Williams. Optimization of eyesafe avalanche photodiode lidar for automobile safety and autonomous navigation systems. *Optical Engineering*, 56:56 – 56 – 9, 2017. 1
- [67] W. Xinwei, L. Youfu, and Z. Yan. Triangular-range-intensity profile spatial-correlation method for 3D super-resolution range-gated imaging. *Applied Optics*, 52(30):7399–406, 2013. 3
- [68] H. Xu, Y. Gao, F. Yu, and T. Darrell. End-to-end learning of driving models from large-scale video datasets. *arXiv preprint*, 2017. 6
- [69] T. Zhou, M. Brown, N. Snavely, and D. G. Lowe. Unsupervised learning of depth and ego-motion from video. In *Proceedings of the IEEE Conference on Computer Vision and Pattern Recognition*, 2017. 2